

Hysteresis Compensation of Flexible Continuum Manipulator using RGBD Sensing and Temporal Convolutional Network

Junhyun Park^{1*}, Seonghyeok Jang^{1*}, Hyojae Park¹, Seongjun Bae², and Minho Hwang^{1†}

Abstract— Flexible continuum manipulators are valued for minimally invasive surgery, offering access to confined spaces through nonlinear paths. However, cable-driven manipulators face control difficulties due to hysteresis from cabling effects such as friction, elongation, and coupling. These effects are difficult to model due to nonlinearity and the difficulties become even more evident when dealing with long and multi-segmented manipulator. This paper proposes a data-driven approach based on recurrent neural networks to capture these nonlinear and previous states-dependent characteristics of cable actuation. We design customized fiducial markers to collect physical joint configurations as a dataset. Result on a study comparing the learning performance of four Deep Neural Network (DNN) models show that the Temporal Convolutional Network (TCN) demonstrates the highest predictive capability. Leveraging trained TCNs, we build a control algorithm to compensate for hysteresis. Tracking tests in task space using unseen trajectories show that the best controller reduces the mean position and orientation error by 61.39% (from 13.7 mm to 5.29 mm) and 64.04% (from 31.17° to 11.21°), respectively.

I. INTRODUCTION

In contrast to rigid surgical robots that navigate lesions through laparoscopic approaches, flexible endoscopic surgical robots can access endoluminal regions by traversing a curved path through natural orifices such as the mouth, anus, and vagina. Due to their heightened accessibility to lesions and clinical advantages of scar-free procedures, a new robotic platform has been actively under investigation [1-4]. These platforms have demonstrated effectiveness in endoscopic tasks like Endoscopic Submucosal Dissection (ESD). However, they lack the necessary degrees-of-freedom (DOF) to execute motions for complex tasks such as tissue suturing and vascular anastomosis. Despite the need for additional DOFs to perform more advanced tasks, challenges arise in designing multi-DOF due to size constraints [5].

* These authors are equally contributed, † Corresponding author.

This work was supported in part by the DGIST R&D Program of the Ministry of Science and ICT (23-PCOE-02, 23-DPIC-20) and by the collaborative project with ROEN Surgical Inc.

This work was supported in part by the Korea Medical Device Development Fund grant funded by the Korea government (the Ministry of Science and ICT, the Ministry of Trade, Industry and Energy, the Ministry of Health & Welfare, the Ministry of Food and Drug Safety) (Project Number: 1711196477, RS-2023-00252244) and by the National Research Council of Science & Technology (NST) grant by the Korea government (MSIT) (CRC23021-000).

¹ J. Park, S. Jang, H. Park, and M. Hwang are with the Department of Robotics and Mechatronics Engineering, DGIST, Daegu, 42988 Korea (e-mail: {sean05071, jshtop1, hyojae, minho} @dgist.ac.kr).

² S. Bae is with the School of Undergraduate Studies, DGIST, Daegu, 42988 Korea (email: twin010528@dgist.ac.kr).

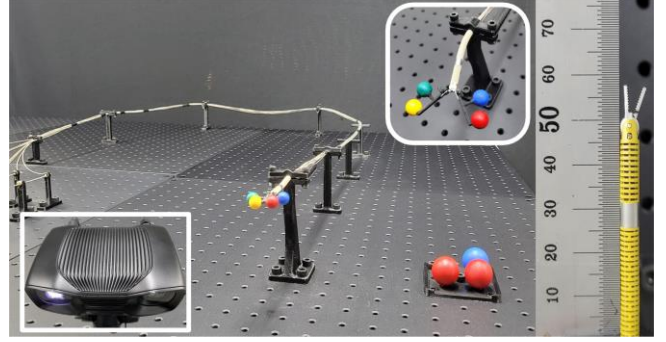


Fig. 1. The 3D printed fiducial markers are attached to the forceps to estimate the physical joint angles of the proposed continuum manipulator. We use a RGBD camera to detect the central position of fiducial marker.

Another significant limitation of the existing platforms is in control inaccuracy due to long and flexible actuation cables. Endoscopic surgical platforms are remotely powered by multiple bundles of Bowden-cables passing through a lengthy flexible tube, exceeding 1.5m in length. The prolonged cable introduces challenges such as friction, twisting [6], extension [7], backlash [8], and coupling [9], leading to uncertainties in the control and hysteresis of the flexible manipulator.

This paper focuses on overcoming the challenges associated with flexible manipulators. To address the constraints imposed by insufficient DOFs, we propose a design of a dual-segment continuum effectively perform endoscopic surgery within confined anatomical spaces. This study includes kinematic analysis and derivation of the cable-driven equation associated with the proposed manipulator.

To improve the control inaccuracies, we adopt a data-driven approach. We attach customized fiducial markers for capturing ground-truth poses of the proposed manipulator using RGBD sensing (See Fig. 1), collecting data to identify the nonlinear features of the hysteresis. The dataset is used to train a deep learning models, enabling the models to predict movements that reflect cabling effects. With the trained model, we design a controller to compensate for the hysteresis.

The main contributions in this paper are summarized as follows: (1) Design of a dual-segment manipulator for flexible endoscopic surgery. (2) Ground-truth state estimation method of the manipulator with forceps based on the 3D-printed fiducial markers. (3) Hysteresis compensation controller applied with TCN model to involve hysteresis effects in a long and flexible instrument. (4) Validation of the proposed controller through tracking tests on unseen trajectories.

The paper is organized as follows: Section II discusses current trends in continuum manipulator research and outlines the distinctive features of our study. In Section III, we delve

into the hinge design, kinematic analysis, and cable drive method employed in the proposed continuum manipulator. Section IV & V introduces hysteresis compensation control methods alongside the utilization of deep learning models and conducts tracking tests to verify the results. Finally, Section VI concludes the paper and suggests directions for future research.

II. RELATED WORKS

Ongoing studies have actively explored dual-segment continuum mechanisms and motions [10-12] to optimize continuum surgical manipulators for intricate tasks. They use rigid instruments to model the continuum segments and thus does not consider flexible power transmission parts in their modeling. C. Zhang et al. [13] introduces a flexible continuum instrument based on elastic flexure for endoscopic surgery, demonstrating its capability in ex-vivo environment. This study reveals aspects that have yet to be addressed, in evaluating the interaction among each segment. While the insertion part is designed for flexibility, this study does not consider performance evaluation within the curved path.

Previous studies on compensating for hysteresis in continuum manipulators have primarily adopted two approaches. Firstly, compensating for hysteresis through analytical modeling [14-17], as seen in Lee et al. [18] work, where they propose a simplified hysteresis model that defined dead zones and backlash. Analytical hysteresis compensation is effective when properties of the hysteresis model are clear and simple. However, as the complexity of the hysteresis model increases, analytical compensating encounters evident limitations. Secondly, studies have employed learning-based approach [19]. Kim et al. [20] propose a study that effectively combines analytical and deep learning models to predict hysteresis variations based on the shape of Tendon-Sheath Mechanism (TSM). They focus on single pair of tendon-sheath to predict the hysteresis model in the curved pathway.

Hwang et al. [21] effectively calibrate the robotic surgical instruments based on deep neural network models. They utilize RGBD cameras and fiducial markers to accurately estimate ground-truth poses of the robot. They deal with a laparoscopic instrument, which is rigid and relatively short.

In this paper, we stand out by introducing an approach to compensate for a more complex hysteresis model of a long flexible endoscopic instrument, including a compensation for forceps motion—a facet not covered in previous research.

III. DESIGN AND ANALYSIS OF CONTINUUM MANIPULATOR

The proposed continuum manipulator is composed of segment 1, segment 2, and a gripper arranged from the proximal to the distal ends. Each segment operates based on flexure-hinge module which is designed to have a maximum bending angle of 10 degrees. The manipulator is equipped with a total of 5 DOFs, comprised of 2 elbow joints, 1 wrist joint, and 2 grippers. We use 10 actuation cables with a length of 2.5m for flexible power transmission connected to the driving unit.

A. Design Considerations

The flexure hinge-based continuum manipulators offer the advantage of miniaturizing due to its simple structure. The specific design parameters are detailed in Table I. (see Fig. 2).

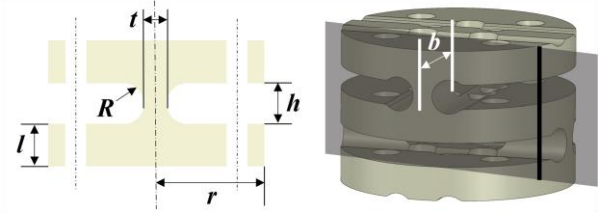


Fig. 2. Design parameters of flexure hinge module: The design of the flexure hinges in the manipulator is based on the Circular Flexure Hinge Design by Paros and Weisbord [22].

TABLE I
DESIGN PARAMETERS OF FLEXURE HINGE MODULE

Parameters	Value
Height between notches, h	0.5mm
Thickness of the disk, l	0.7mm
Round radius of the hinge, R	0.35mm
Front thickness, t	0.4mm
Side thickness of the hinge, b	1.3mm
Radius of module, r	2.4mm

Finite element analysis is conducted to confirm the suitability of the flexure hinge design made of PEEK. The simulation is performed on a single hinge model, and the global mesh size is 0.1mm and the local mesh size for the bending center is 0.02mm, so the total number of elements is 350746. For boundary conditions, the bottom side is designated as fixed support, the force due to driving cable is 1.9 N, and the friction coefficient for the contact surface is 0.3. As a result of the analysis, the bending angle for a single hinge model is 5.5°, and the maximum strain is 0.0378mm/mm. The number of reversals was reported as 18454 to 92078 when the strain amplitudes were carried out at 0.5Hz between 0.04mm/mm and 0.035mm/mm [23]. This generally corresponds to a high cycle life, ranging from 10^4 to 10^6 . The proposed manipulator consists of a total of 11 hinge modules to have a high cycle life even if reciprocating with an amplitude of 60.5°.

B. Kinematics Analysis of Continuum Manipulator

The composition of the proposed manipulator is described in Fig. 3. The bending motion of a flexure-hinge module can be assumed to involve two identically rotating revolute joints and one prismatic joint. Table II provides parameters for a single module of segment 1 based on the Modified Denavit-Hartenberg convention. The symbols θ_p , θ_y in Table II denote the bending angles in the pitch, and yaw direction, respectively. Additionally, the bending angle Tr_i in Table II is calculated using the following relationship (see Fig.4):

$$Tr_i = b \cdot \cos\left(\frac{\theta_i}{2}\right) + \frac{2h}{\theta} \sin\left(\frac{\theta_i}{2}\right) \quad (1)$$

The transformation matrix between adjacent equivalent joints can be expressed as follows.

$${}^{k-1}T_k = \begin{bmatrix} c\theta_k & -s\theta_k & 0 & a_{k-1} \\ s\theta_k c\alpha_{k-1} & c\theta_k c\alpha_{k-1} & -s\alpha_{k-1} & -d_k s\alpha_{k-1} \\ s\theta_k s\alpha_{k-1} & c\theta_k s\alpha_{k-1} & c\alpha_{k-1} & d_k c\alpha_{k-1} \\ 0 & 0 & 0 & 1 \end{bmatrix} \quad (2)$$

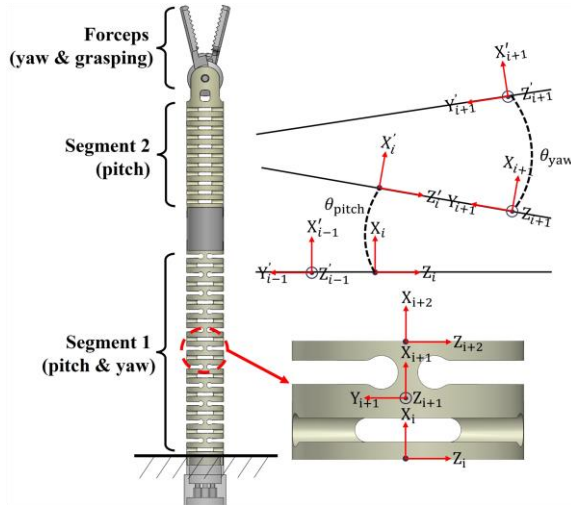


Fig. 3. Manipulator Components and Coordinate System for a Single Module of Segment 1: The proposed manipulator is constructed by connecting modules of segment 1 capable of bending in the pitch-yaw direction and modules of segment 2 that can bend in the pitch direction. The forceps can grasp and rotate yaw-direction.

TABLE II: KINEMATICS PARAMETERS ACCORDING TO DENAVIT-HARTENBERG CONVENTION FOR ONE HINGE MODULE OF SEGMENT 1

	Number of coordinate frame							
	1	2	3	4	5	6	7	8
α_{k-1}	$\pi/2$	0	0	0	$-\pi/2$	0	0	0
a_{k-1}	0	0	Tr_i	0	0	0	Tr_{i+1}	0
d_k	0	0	0	0	0	0	0	0
θ_k	0	$\theta_p/2$	0	$\theta_p/2$	0	$\theta_y/2$	0	$\theta_y/2$

where $c\theta_k$, $s\theta_k$, $c\alpha_k$, and $s\alpha_k$ are $\cos(\theta_k)$, $\sin(\theta_k)$, $\cos(\alpha_k)$, and $\sin(\alpha_k)$, respectively. The transformation matrix for a single module of segment 1 is acquired by multiplying coordinate systems from 1 to 8 in Table II. Similarly, for segment 2's module, it is obtained by multiplying coordinate systems from 2 to 4 in Table II.

$${}^0T_n = {}^0T_1 {}^1T_2 {}^2T_3 \dots {}^{k-1}T_k \dots {}^{n-2}T_{n-1} {}^{n-1}T_n \quad (3)$$

Concatenating the coordinate systems of all 11 single modules of segment 1 makes the position and orientation of segment 1 (elbow). For segment 2, employ a similar process to interconnect all modules. Ultimately, by multiplying all transformation matrices by considering the rotation of the forceps, the transformation matrix from base to end-effector can be obtained.

C. Cable Drive Equation

Fig. 5(b) depicts the geometric relationship showing cable variations during bending at each joint angle. The change in actuating cable length can be expressed as follows.

$$\Delta w_i(\theta_i, d_i) = \left(\frac{H \cdot n}{\theta_i} - \frac{d_i}{2} \right) \cdot 2 \cdot \sin \frac{\theta_i}{2n} \quad (i=1, \dots, n) \quad (4)$$

where Δw_i is the variation in cable length, H is the length between notches, θ_i is the angle at which each hinge bends,

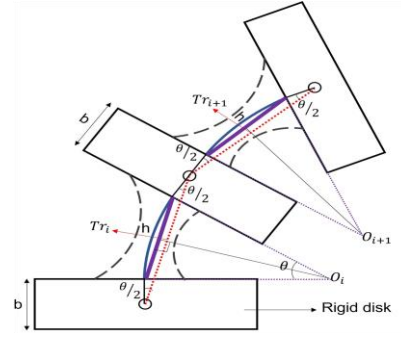


Fig. 4. Geometric depiction of the flexure hinge module: The hinge module bends in the θ direction, causing a change in the length of Tr_i .

and n is the total number of hinges. We control an antagonistic pair of cables to drive a joint based on equation (4) (see Fig. 5). Additionally, we consider decoupling for wrist and gripper control affected by segment bending. Namely, when segment 1 bends in the pitch direction, cables w_5 and w_6 , controlling segment 2, are adjusted by pulling or releasing them in response to the bending of segment 1.

IV. HYSTERESIS MODELING AND COMPENSATION

Due to the hysteresis, there exist a discrepancy between the command joint configuration, \mathbf{q}_{cmd} , and the physical joint configuration, \mathbf{q}_{phy} . To model the hysteresis, we measure \mathbf{q}_{phy} in accordance with \mathbf{q}_{cmd} using fiducial markers and RGBD (see Fig. 6). In this section, we describe a learning-based method for modeling cabling effects and a controller to compensate for the hysteresis using the trained model.

A. Estimation of Physical Joint Configuration

We obtain the position and orientation of the base and end effector of the prototyped manipulator using colored sphere fiducials (see Fig. 7). We designed the arrangement of markers with different offsets to avoid occlusion in various poses. We assign two spheres to each forceps to measure the gripper angle. The transformation matrix from the camera to the base through the positions of the center points of the three spheres is obtained as follows.

$$T_{base}^{cam} = \begin{bmatrix} R_{base}^{cam} & P_{base}^{cam} \\ 0 & 1 \end{bmatrix} = \begin{bmatrix} \hat{x}_B^T & \hat{y}_B^T & \hat{z}_B^T & p_{base}^{cam} \\ 0 & 0 & 0 & 1 \end{bmatrix} \quad (5)$$

where

$$\begin{cases} \hat{x}_B = \hat{y}_B \times \hat{z}_B \\ \hat{y}_B = \mathbf{v}_{r_0}^{r_1} / \|\mathbf{v}_{r_0}^{r_1}\| \\ \hat{z}_B = \mathbf{v}_{r_1}^{b_0} / \|\mathbf{v}_{r_1}^{b_0}\| \\ p_{base}^{cam} = (p_{r_0} + p_{r_1})/2 + L_{base} \end{cases} \quad (6)$$

In equation (6), the subscripts B with x , y , z denotes the base, while the subscripts r_0 , r_1 , and b_0 represent the color and number of the sphere and maintain the same notation throughout. L_{base} is the offset between the robot base and the base marker. Next, we determine the orientation and position

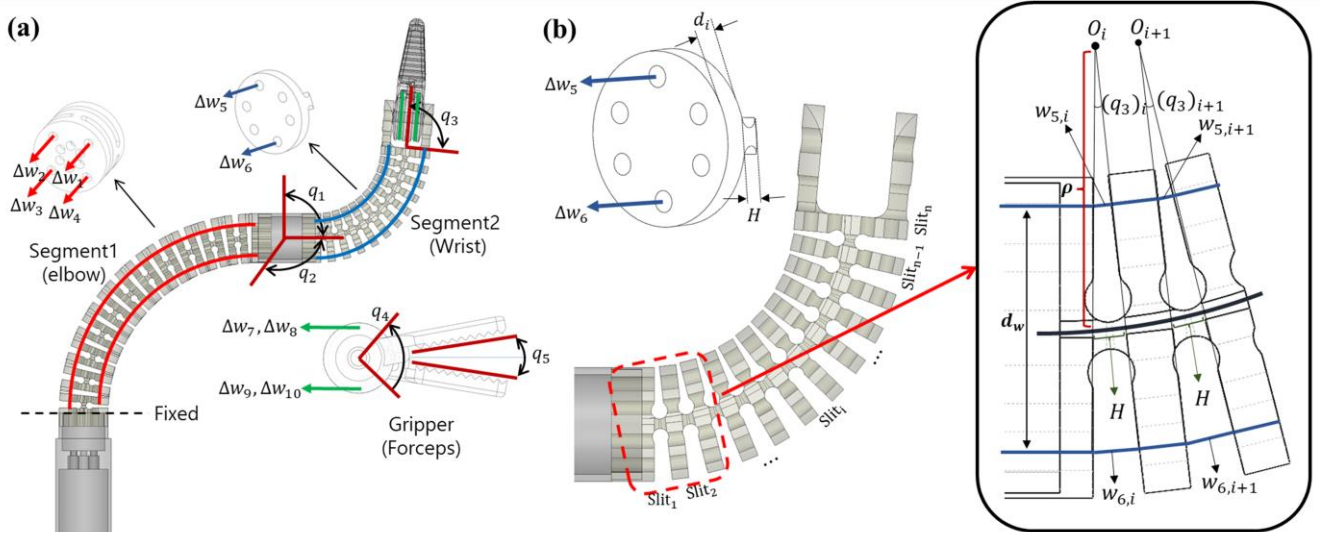


Fig. 5. DOFs configuration and cable relationships in the proposed continuum manipulator: (a) Description of the individual DOFs (q_1, q_2, q_3, q_4 , and q_5) for manipulator. Specifically, segment 1 (elbow) has 2 DOFs for pitch and yaw direction bending, driven by cables w_{1-4} , denoted as q_1 and q_2 , segment 2 (wrist) has 1 DOFs for pitch direction bending, driven by cables $w_{5,6}$, represented as q_3 and the gripper (forceps) is equipped with 2 DOFs, driven by cables w_{7-10} , for yaw direction rotation (q_4) and grasping (q_5), (b) Geometric representation of cable variations w_i during the bending of adjacent hinge (Magnified view of the red-boxed region showing an ideally bent segment 2).

for the forceps₁ (left) and represent the homogeneous transformation matrix as follows.

$$T_{fcps_1}^{cam} = \begin{bmatrix} R_{fcps_1}^{cam} & P_{fcps_1}^{cam} \\ 0 & 1 \end{bmatrix} = \begin{bmatrix} \hat{x}_{f_1}^T & \hat{y}_{f_1}^T & \hat{z}_{f_1}^T & P_{fcps_1}^{cam} \\ 0 & 0 & 0 & 1 \end{bmatrix} \quad (7)$$

where

$$\begin{cases} \hat{x}_{f_1} = v_{r_2}^{b_1} / \|v_{r_2}^{b_1}\| \times v_{y_0}^{b_1} / \|v_{y_0}^{b_1}\| \\ \hat{y}_{f_1} = (\hat{x}_{f_1} \times \hat{z}_{f_1}) \\ \hat{z}_{f_1} = v_{b_1}^{r_2} / \|v_{b_1}^{r_2}\| \\ P_{fcps_1}^{cam} = p_{b_1} + L_{fcps_1} \end{cases} \quad (8)$$

$$R_{fcps_1}^{cam} = R_x(\psi) \cdot R_{fcps_1}^{cam} \quad (9)$$

In equation (8) and (9), the subscripts f_i with x, y, z and $fcps_1$ denote the forceps₁ and ψ represents the angle resulting from an offset design aimed at reducing marker occlusion. The position and orientation of forceps₂ (right) can be obtained the same as forceps₁. The orientation and position of the end-effector can be obtained as follows.

$$\theta = (\cos^{-1}(\hat{z}_{f_1} \cdot \hat{z}_{f_2})) / 2 \quad (10)$$

$$R_{EE}^{cam} = R_x(\theta/2) \cdot R_{fcps_1}^{cam} \quad (11)$$

$$p_{EE}^{cam} = (p_{fcps_1}^{cam} + p_{fcps_2}^{cam}) / 2 + (d_{fcps_1} - d_{fcps_1} \cdot \cos(\theta/2)) \cdot \hat{z}_{f_1} \quad (12)$$

$$T_{EE}^{base} = (T_{EE}^{cam})^{-1} \times T_{EE}^{cam} \quad (13)$$

where θ denote the angle between forceps₁ and forceps₂ and d_{fcps_1} denote the distance from the rotation center to the end of forceps₁. From the equation (13), we calculate T_{EE}^{base} and we apply inverse kinematics to obtain the joint configuration.

B. Dataset Collection and Hysteresis Observation

It is effective to model and control hysteresis in joint space because the cabling effect has joint-specific attributes. To construct the command trajectory, we initiate the process by randomly selecting joint configurations within joint limits. The interpolation ensures equal distances in the joint space, as expressed in equation (14), where q_{p_1} and q_{p_2} represent two randomly selected points.

$$\bar{q}_{kth\ inter} = \bar{q}_{p_1} + k \cdot \frac{(\bar{q}_{p_1} - \bar{q}_{p_2})^T (\bar{q}_{p_1} - \bar{q}_{p_2})}{3\sqrt{5}} \times (\bar{q}_{p_1} - \bar{q}_{p_2}) \quad (14)$$

We create a dataset, denoted as \mathcal{D} in equation (15), where \mathcal{D} comprises 30,707 command joint configurations (q_{cmd}) and their corresponding physical joint configurations (q_{phy}). q_{cmd} are uniformly separated by 3° through the interpolation process, and the q_{phy} are captured using fiducial markers and RGBD sensing.

$$\mathcal{D} = \left((q_{cmd}, q_{phy}) \right)_{t=1, 2, 3, \dots, 30,707} \quad (15)$$

A notable nonlinear difference between q_{phy} and q_{cmd} is evident (see Fig. 8 (a)), and the corresponding statistics are summarized in Table III. q_{phy} exhibits a subtle rightward offset compared to q_{cmd} in Fig. 8(a). Fig. 8(b) illustrates a hysteresis of q_1 and q_3 , where the observed irregularities indicate the challenge of modeling hysteresis in analytic form.

C. Hysteresis Modeling using Deep Learning

We employ two approaches using four architectures: the forward approach (f_θ) and the inverse approach (f_θ^{-1}). The forward approach predicts physical joint configuration from prior commanded configurations, while the inverse approach predicts commanded configurations from prior physical joint states. In mathematical terms,

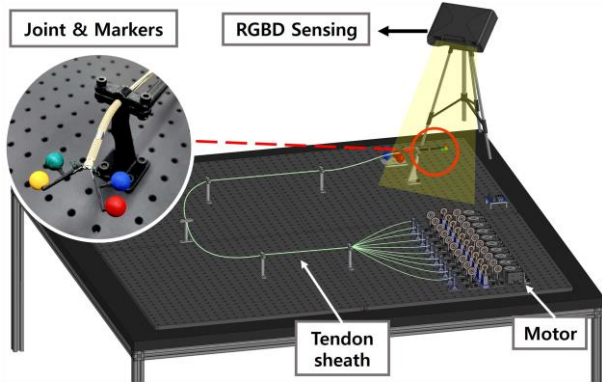


Fig. 6. Schematic illustration of manipulators with fiducial markers and RGBD sensing: the prototyped manipulator with 4.8 mm in diameter and 2.5 m in length. Seven fiducial markers are affixed to capture the orientation and position of the manipulator's base and end-effector.

$$\text{Forward: } \hat{q}_{phy}^t = f_{\theta}(\mathbf{q}_{cmd}^{(t, t-1, t-2, \dots, t-L)}) \quad (16)$$

$$\text{Inverse: } \hat{q}_{cmd}^t = f_{\theta}^{-1}(\mathbf{q}_{phy}^{(t, t-1, t-2, \dots, t-L)}) \quad (17)$$

where L is the length of input sequence.

Architectures: We contemplate the subsequent candidate architectures for f_{θ} and f_{θ}^{-1} . All architectures share common parameters, including a 0.001 learning rate, 32 batch size, Mean Square Error (MSE) loss functions, and the utilization of the Adam optimizer for training.

MLP: A multi-layer perceptron featuring three hidden layers, each comprising 128 units.

LSTM: A long-short term memory structure [24] with 128 units, followed by two linear layers, each containing 64 units.

TCN: A temporal convolutional network [25] characterized by multiple residual blocks, each block consists of two 1-dimensional dilated causal convolution layers, accompanied by weight normalization. The number of residual blocks is determined by the input sequence length, adopting a dilatation base of 2 and convolutional kernel size of 3.

TCN- LSTM: A TCN-LSTM model is hybrid model incorporating TCN and LSTM. The feature extracted by the TCN serve as input to an LSTM layer. This hybrid model outperforms individual TCN and LSTM models, particularly in predicting network traffic [26] and particulate matter concentration [27].

To facilitate the training of the 8 models, we partition \mathcal{D} into an 80% training set (24,565 pairs) and a 20 % test set (6,142 pairs). The training process is conducted on an RTX 3070 graphics card, with each model undergoing training for 8000 epochs. Considering hysteresis dependence on historical states, we vary input sequence lengths ($L = 10, 50, 65, 80, 100, 120$) to identify optimal lengths. Each of the eight models is trained three times and mean and standard deviation of validation Root Mean Square Error (RMSE) are computed for each model (Fig. 9 & Fig. 10). The TCN at $L = 80$ exhibits superior performance for both forward and inverse approaches with the lowest standard deviation and loss. While TCN-LSTM generally exhibits better performance, TCN demonstrated optimal estimation performance in the corresponding task.

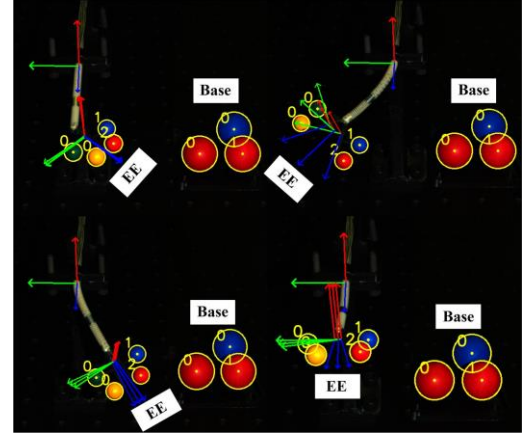
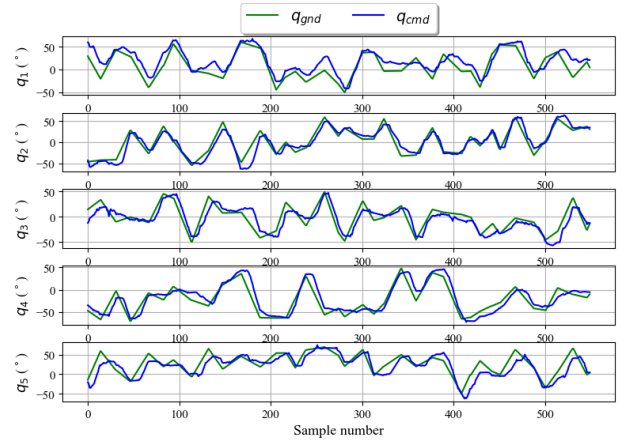
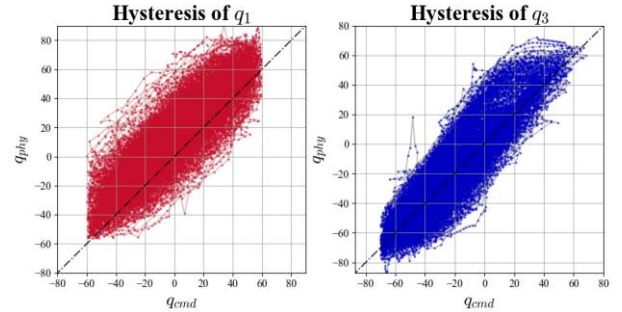


Fig. 7. Fiducial Marker Detection: Utilizing larger red and blue markers for base position and orientation calculation, and smaller red, blue, yellow, and green markers for orientation and position of forceps (forceps_1 , forceps_2). Central point estimation achieved through a non-linear regression process based on point cloud data [21].



(a) Plotting \mathbf{q}_{cmd} and \mathbf{q}_{phy} in joint space



(b) Hysteresis model for \mathbf{q}_1 and \mathbf{q}_3

Fig. 8. The Comparison of the Command and the Physical Joint Configurations Throughout Collected Dataset \mathcal{D} : (a) The plot of command and physical joint angles for a random trajectory, (b) Hysteresis model for command and physical values (\mathbf{q}_1 , \mathbf{q}_3).

TABLE III: MEAN ABSOLUTE ERROR AND STANDARD DEVIATION BETWEEN PHYSICAL AND COMMAND JOINT CONFIGURATION

	Joint angle				
	q1(°)	q2(°)	q3(°)	q4(°)	q5(°)
MAE	16.31	10.09	11.21	12.02	13.84
SD	11.59	7.67	7.56	8.91	10.37

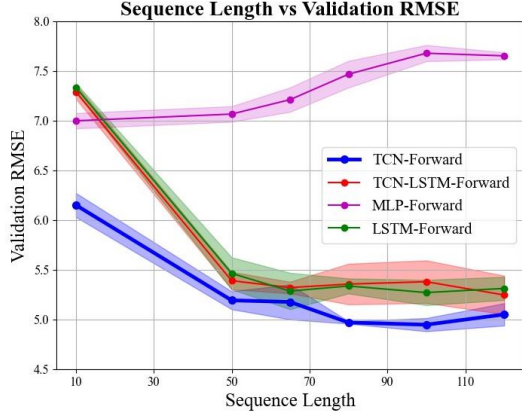


Fig. 9. Validation RMSE for Varying Input Sequence Length in Forward Model: The recorded RMSE values are presented, with line width indicating standard deviation. Convergence initiates for most models at $L = 50$. TCN exhibits optimal performance across overall sequence inputs, whereas TCN-LSTM and LSTM exhibit comparable performance.

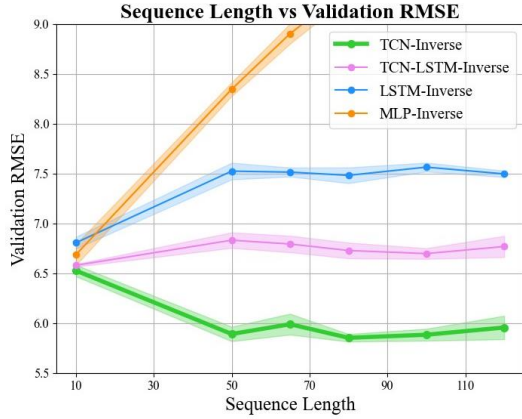


Fig. 10. Validation RMSE for Varying Input Sequence Length in Inverse Approach: The recorded RMSE values are presented, with line width indicating standard deviation. Most models begin to converge at $L = 50$, but the MLP model struggles to effectively discern features with an increase of sequence length.

D. Design of Hysteresis Compensation Controller

The trained inverse model, capable of estimating command joint configurations from prior physical joint configurations, enables direct acquisition of the calibrated command by inputting the desired joint configuration. However, as seen in Fig. 9 and Fig. 10, the inverse approach models exhibit lower accuracy compared to the forward approach models. Consequently, both forward and inverse approaches are integrated into the controller for enhanced accuracy. Optimal performance models, specifically TCN at $L = 80$ in both approaches, are selected, trained multiple times, and ensembled to improve stability. This controller takes the desired joint configuration $\mathbf{q}_{desired}^{(t)}$ as input and computes the command joint configuration, which can align the robot with the $\mathbf{q}_{desired}^{(t)}$. The algorithm for this controller (Algorithm 1) initiates the command using TCN-inverse (f_{θ}^{-1}) and refines it iteratively based on the error between desired position and TCN-forward estimation (f_{θ}). The initialization ensures accurate convergence utilizing $f_{\theta}^{-1}(\mathbf{q}_{desired}^{(t,t-1,...,t-L)})$. The

Algorithm 1 Hysteresis Compensation Algorithm

Require: Desired joint angle $\mathbf{q}_{desired}^{(t)}$, robot state estimator f_{θ} , command estimator f_{θ}^{-1} , number of iterations M , learning rate α , time sequence length L , loss threshold Thr , joint size Q

- 1: $\mathbf{q}_{calibrated}^{(t)} \leftarrow f_{\theta}^{-1}(\mathbf{q}_{desired}^{(t,t-1,...,t-L)})$
- 2: **for** iteration $\in \{1, \dots, M\}$
- 3: loss $\leftarrow \mathbf{q}_{desired}^{(t)} - f_{\theta}(\mathbf{q}_{calibrated}^{(t,t-1,...,t-L)})$
- 4: **for** idx $\in \{1, \dots, Q\}$
- 5: **do if** loss[idx] $> Thr$
- 6: **then** $\mathbf{q}_{calibrated}^{(t)}[idx] \leftarrow \mathbf{q}_{calibrated}^{(t)}[idx] - \alpha \cdot \text{loss}$
- 7: **return** $\mathbf{q}_{calibrated}^{(t)}$

algorithm evaluates the forward dynamics to estimate the physical joint configuration ($f_{\theta}(\mathbf{q}_{calibrated}^{(t,t-1,...,t-L)})$). It then calculates the error and updates the command if the error exceeds a predefined loss threshold.

V. RESULTS AND VALIDATION

A. Trajectory Tracking Test

To evaluate the performance of the proposed hysteresis compensation controller, a tracking experiment was conducted on three trajectories in task space. In configuring the controller for the proposed manipulator, parameters are set as $Q = 5$, $M = 50$, $\alpha = 0.001$, and $Thr = 4$. Considering that the TCN-forward at $L = 80$ displays a validation loss of 5.0, we set the Thr at 4. We use three unseen trajectories with random, circular, and zigzag patterns. Errors and standard deviations are calculated by performing the trajectory five times.

The tracking performance across different target trajectories is visualized in Fig. 11, with detailed mean absolute error and standard deviation values for position and orientation presented in Table IV. The results of the uncalibrated control, conducted through cable-driven control mentioned in Section III, resulted in a substantial mean error of 13.70 mm for the three trajectories. In comparison, the calibrated control significantly reduced the error to 5.29 mm based on feedback using the deep learning model. The mean position error and standard deviation of the position error were approximately 61% and 54% lower than the uncalibrated control, respectively.

Notably, the forceps movement shows significant improvement in zigzag trajectory, as illustrated in Fig. 12. The uncalibrated control indicated lack of precision due to widened dead zone by amplified cable effects. However, calibrated control effectively compensates nonlinear hysteresis in intricate movements. The specific statistics of the tracking error are documented in Table V. The joint angle errors at zigzag trajectory are reduced by 70.06%, 53.61%, 42.02%, 54.18%, and 63.04% in q_1, q_2, q_3, q_4 , and q_5 , respectively.

VI. CONCLUSION

In this paper, we proposed a 5-DOF flexible manipulator, with a diameter of 4.8mm and length of 2.5m, which can be

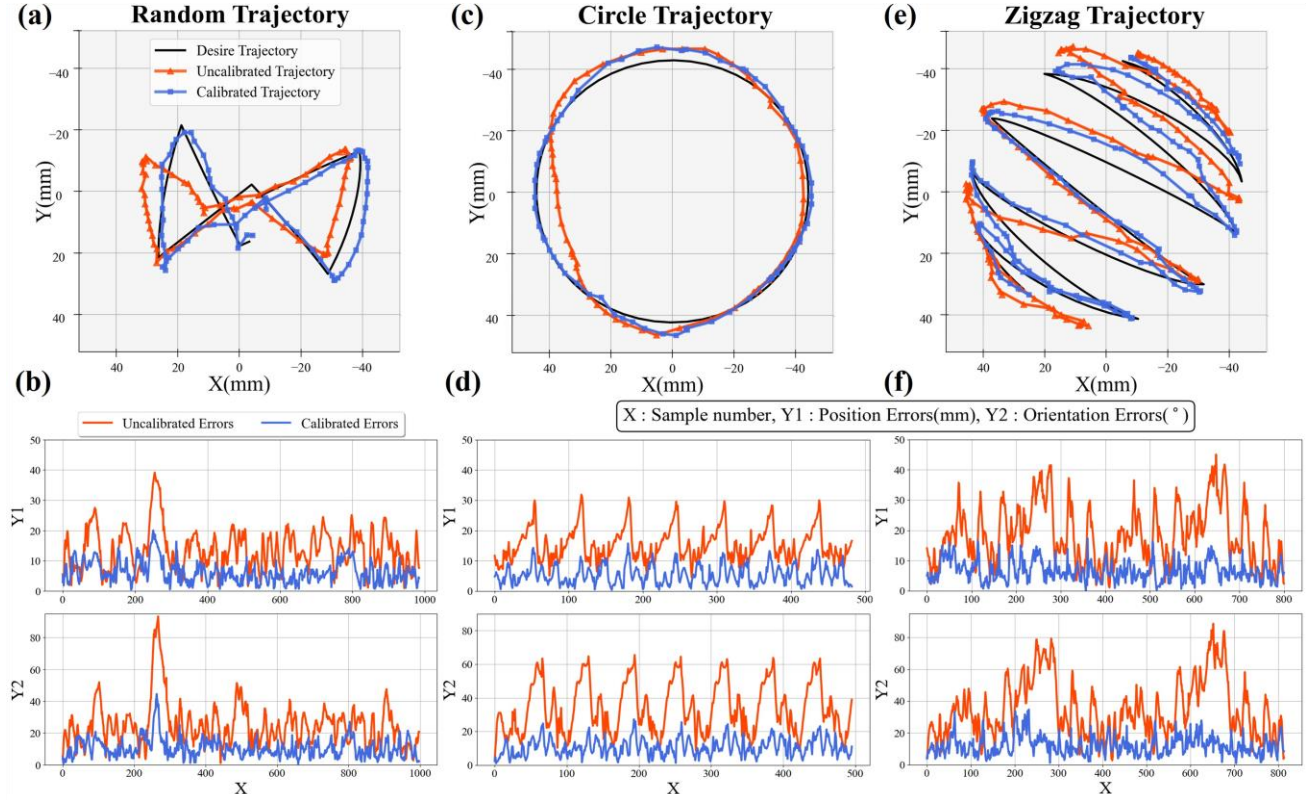


Fig. 11. The figures illustrate how both uncalibrated and calibrated controllers perform in terms of tracking and errors during trajectory tracking tests: Subfigures (a)-(b) show performance and errors on a random trajectory, while (c)-(d) demonstrate performance and errors on a circular trajectory and lastly (e)-(f) show performance and errors on a zigzag trajectory. Before calibration, errors in random trajectories show unpredictable deviations overall. In the circular trajectory, the error indicated a repetitive pattern of increasing values over a particular interval. In the zigzag trajectory, the error revealed the most inconsistent large deviation. However, after calibration, all trajectories showed a significantly reduced and uniform deviation. For visibility, only specific parts of the trajectories are shown in (a), (c), and (e).

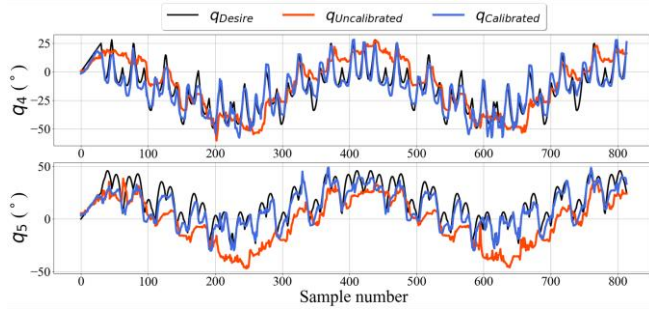
TABLE IV: POSITION AND ORIENTATION ERRORS AND STANDARD DEVIATIONS FOR UNCALIBRATED AND CALIBRATED CONTROL ACROSS MULTIPLE TRAJECTORIES IN TASK SPACE

MAE	Trajectory							
	Random		Circle		Zigzag		Mean value	
	Uncalibrated	Calibrated	Uncalibrated	Calibrated	Uncalibrated	Calibrated	Uncalibrated	Calibrated
X Error (mm)	7.44	3.27	6.66	2.31	8.84	2.66	7.65	2.75
Y Error (mm)	7.39	3.60	7.04	2.48	7.34	3.40	7.26	3.16
Z Error (mm)	5.54	2.44	9.34	3.62	11.37	3.63	8.75	3.23
Total position error (mm)	11.86	5.47	13.46	4.96	16.16	5.64	13.70	5.29
Standard deviation	6.80	3.50	5.40	3.08	9.36	3.29	7.19	3.29
Orientation Error (°)	24.74	10.41	33.88	10.65	34.89	12.58	31.17	11.21
Standard deviation	13.94	5.90	15.18	5.10	18.09	5.86	15.74	5.62

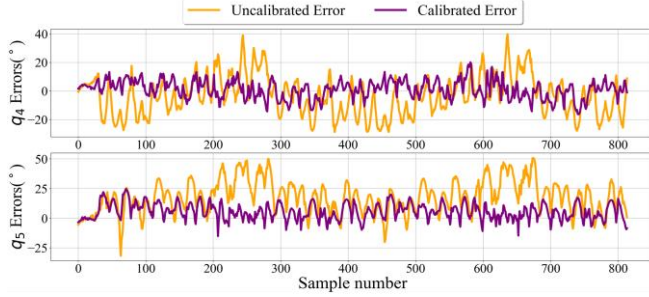
utilized for endoscopic surgeries in confined space. However, the designed manipulator accompanies significant hysteresis due to factors such as friction, cable elongation, and coupling. To model these nonlinearities, we introduce a deep learning-based method. We collect joint angle data from the robot using an RGBD camera and seven fiducial markers. With the collected dataset, we train TCN-inverse and forward models, creating a TCN-based hysteresis compensation control algorithm. Trajectory tracking tests on unseen trajectories shows a notable reduction in mean position and orientation errors in task space—approximately 61.39%, from 13.70mm to 5.29mm, and 64.04%, from 31.17° to 11.21°, respectively. Despite the hysteresis effects, the proposed controller demonstrated the reduced error and

deviation (see Fig. 11(b), (d), (f)). The observed improvement is expected to improve performance of surgical tasks by reducing position errors in long cable-connected continuum manipulators.

There exist several limitations during data collection procedure. The trade-off between data quantity for improved model performance and time efficiency challenges due to the low sampling rate of RGBD sensing. To address this, we prioritized efficiency, utilizing 30,707 dataset pairs for training. Future work aims to develop a model achieving superior estimation performance with fewer datasets for more precise control. Additionally, fiducial markers experienced occlusion issues in specific configurations, prompting us to modify the marker supporter design to minimize occlusion.



(a) The comparison of tracking performance for q4 and q5 in joint space



(b) The comparison of tracking error for q4 and q5 in joint space

Fig. 12. Enhanced results in forceps angle (q_4 , q_5) at the joint space (Zigzag trajectory)

TABLE V: JOINT ANGLE ERRORS AND STANDARD DEVIATIONS UNDER UNCALIBRATED AND CALIBRATED CONTROL AT ZIGZAG TRAJECTORY

		Joint Angle Errors				
		q1(°)	q2(°)	q3(°)	q4(°)	q5(°)
Uncalibrated control	MAE	15.60	13.73	12.97	11.37	18.91
	SD	11.42	10.54	8.50	8.19	12.15
Calibrated control	MAE	4.67	6.37	7.52	5.21	6.99
	SD	3.96	4.80	5.82	3.80	5.39

Although these modifications reduced occlusion, it persisted, leading to post-processing like interpolation and outlier elimination. In future efforts, we plan to further optimize the fiducial marker design to decrease occlusion during the detection procedure.

REFERENCES

- [1] M. Hwang and D. Kwon, "K-FLEX: A flexible robotic platform for scar-free endoscopic surgery," in *Int. J. Med. Robotics Comput. Assist. Surg.*, vol. 16, no. 2, pp. e2078, Apr. 2020.
- [2] M. Remacle, *et al.*, "Transoral robotic surgery (TORS) with the Medrobotics FlexTM System: first surgical application on humans," in *Eur. Arch. Oto-Rhino-Laryngol.*, vol. 272, pp. 1451–1455, Feb. 2015.
- [3] S. J. Phee, *et al.*, "Master and slave transluminal endoscopic robot (MASTER) for natural orifice transluminal endoscopic surgery," in *2009 Annu. Int. Conf. IEEE Eng. Med. Biol. Soc.*, Minneapolis, 2009, pp. 1192–1195. (in USA)
- [4] L. Zorn, *et al.*, "A Novel Telemanipulated Robotic Assistant for Surgical Endoscopy: Preclinical Application to ESD," in *IEEE Trans. Biomed. Eng.*, vol. 65, no. 4, pp. 797–808, Apr. 2018.
- [5] T. Da Veiga, *et al.*, "Challenges of continuum robots in clinical context: a review," in *Prog. Biomed. Eng.*, vol. 2, no. 3, pp. 032003, 2020.
- [6] D. Ji, *et al.*, "Analysis of twist deformation in wire-driven continuum surgical robot," in *Int. J. Control Autom. Syst.*, vol. 18, no. 1, pp. 10–20, 2020.
- [7] M. M. Dalvand, *et al.*, "An analytical loading model for n-Tendon continuum robots," in *IEEE Trans. Robot.*, vol. 34, no. 5, pp. 1215–1225, Oct. 2018.
- [8] H. Kim, *et al.*, "Effect of backlash hysteresis of surgical tool bending joints on task performance in teleoperated flexible endoscopic robot," in *Int. J. Med. Robotics Comput. Assist. Surg.*, vol. 16, no. 1, pp. e2047, 2020.
- [9] L. Roy, *et al.*, "Modeling and estimation of friction, extension, and coupling effects in multisegment continuum robots," in *IEEE/ASME Trans. Mechatronics*, vol. 22, no. 2, pp. 909–920, Apr. 2017.
- [10] A. Bajo, *et al.*, "Integration and preliminary evaluation of an insertable robotic effectors platform for single port access surgery," in *2012 IEEE Int. Conf. Robot. Autom.*, Saint Paul, 2012, pp. 3381–3387. (in USA)
- [11] W. Zeng, *et al.*, "Motion Coupling Analysis for the Decoupled Design of a Two-Segment Notched Continuum Robot," in *2021 IEEE Int. Conf. Robot. Autom. (ICRA)*, Xian, 2021, pp. 7665–7671, 2021. (in China)
- [12] W. Hong, *et al.*, "Development and validation of a two-segment continuum robot for maxillary sinus surgery," in *Int. J. Med. Robotics Comput. Assist. Surg.*, vol. 18, no. 1, pp. e2340, 2022.
- [13] C. Zhang, *et al.*, "Flexible endoscopic instrument for diagnosis and treatment of early gastric cancer," in *Med. Biol. Eng. Comput.*, pp. 1–14, 2023.
- [14] T. N. Do, *et al.*, "Hysteresis modeling and position control of tendon-sheath mechanism in flexible endoscopic systems," in *Mechatronics*, vol. 24, no. 1, pp. 12–22, 2014.
- [15] T. N. Do, *et al.*, "Nonlinear friction modelling and compensation control of hysteresis phenomena for a pair of tendon-sheath actuated surgical robots," in *Mech. Syst. Signal Process.*, vol. 60, pp. 770–784, 2015.
- [16] T. Kato, *et al.*, "Tendon-driven continuum robot for neuroendoscopy: validation of extended kinematic mapping for hysteresis operation," in *Int. J. Comput. Assist. Radiol. Surg.*, vol. 11, pp. 589–602, 2016.
- [17] Y. H. Kim and T. Mansi, "Shape-Adaptive Hysteresis Compensation for Tendon-Driven Continuum Manipulators," in *arXiv preprint arXiv:2109.06907*, 2021.
- [18] D. H. Lee, *et al.*, "Non-linear hysteresis compensation of a tendon-sheath-driven robotic manipulator using motor current," in *IEEE Robot. Autom. Lett.*, vol. 6, no. 2, pp. 1224–1231, 2021.
- [19] X. Wang, *et al.*, "A survey for machine learning-based control of continuum robots," in *Front. Robot. AI*, vol. 8, pp. 730330, 2021.
- [20] D. Kim, *et al.*, "Recurrent neural network with Preisach model for configuration-specific hysteresis modeling of tendon-sheath mechanism," in *IEEE Robot. Autom. Lett.*, vol. 7, no. 2, pp. 2763–2770, 2022.
- [21] M. Hwang, *et al.*, "Efficiently calibrating cable-driven surgical robots with RGBD fiducial sensing and recurrent neural networks," in *IEEE Robot. Autom. Lett.*, vol. 5, no. 4, pp. 5937–5944, 2020.
- [22] Y. M. Tseytlin, "Notch flexure hinges: an effective theory," in *Rev. Sci. Instrum.*, vol. 73, no. 9, pp. 3363–3368, 2002.
- [23] R. Shrestha, *et al.*, "Cyclic deformation and fatigue behavior of polyether ether ketone (PEEK)," in *Int. J. Fatigue*, vol. 82, pp. 411–427, 2016.
- [24] S. Hochreiter and J. Schmidhuber, "Long short-term memory," in *Neural Comput.*, vol. 9, no. 8, pp. 1735–1780, 1997.
- [25] S. Bai, *et al.*, "An empirical evaluation of generic convolutional and recurrent networks for sequence modeling," in *arXiv preprint arXiv:1803.01271*, 2018.
- [26] J. Bi, *et al.*, "A hybrid prediction method for realistic network traffic with temporal convolutional network and LSTM," in *IEEE Trans. Autom. Sci. Eng.*, vol. 19, no. 3, pp. 1869–1879, 2021.
- [27] Y. Ren, *et al.*, "Deep learning coupled model based on TCN-LSTM for particulate matter concentration prediction," in *Atmos. Pollut. Res.*, vol. 14, no. 4, pp. 101703, 2023.